Highly Photo-Responsive $LaTiO_2N$ Photoanodes by Improvement of Charge Carrier Transport among Film Particles

Jianyong Feng, Wenjun Luo, Tao Fang, Hao Lv, Zhiqiang Wang, Jian Gao, Wenming Liu, Tao Yu, Zhaosheng Li, and Zhigang Zou*

With a theoretical maximum photocurrent of ca. 12.5 mA cm^{-2} under AM 1.5 G 100 mW cm^{-2} irradiation, the presently achieved plateau photocurrent of about 0.6 mA cm^{-2} on bare $LaTiO_2N$ photoanodes indicates the presence of serious charge transport limitations. Only recently, a plateau photocurrent of about 4 mA cm^{-2} was achieved on precious IrO_2 modified $LaTiO_2N$ photoanodes prepared by a rather expensive and complex method, without discussing the intrinsic mechanism of improved photocurrents. In this study, by establishing highly crystalline porous $LaTiO_2N$ particles and superior inter-particle connectivity with reduced density of grain boundaries among the film particles, a record plateau photocurrent of 6.5 mA cm^{-2} on the Co_3O_4 modified $LaTiO_2N$ photoanodesis demonstrated under AM 1.5 G 100 mW cm^{-2} simulated sunlight. More broadly, this work shows the intrinsic requirements and significance of constituting (oxy)nitride particles for efficient charge transport and therefore desirable photoelectrochemical performances on the (oxy)nitride photoelectrodes, which have never been noticed and investigated before. With the obtained rules to follow are encouraging to explore the remaining substantial (oxy)nitride semiconductors as potential photoelectrodes for solar energy conversion.

1. Introduction

Abundant but intermittent solar energy can be stored in the form of chemical energy via photoelectrochemical (PEC) water splitting, which represents an attractive prospect for solving the increasingly serious energy crisis and environmental problems.[1] The pioneering work on the TiO_2 photoelectrode[2] has fueled significant research activity focused on visible-light responsive metal oxide photoelectrodes such as Fe_2O_3,[3] WO_3,[4] and $BiVO_4$,[5] because of their good photostabilities. Recently, (oxy)nitrides,[6] especially Ta_3N_5,[7] $LaTiO_2N$,[8a] and $SrNbO_2N$,[8b] have attracted considerable interest because they meet several criteria for efficient PEC water splitting, such as high theoretical solar-to-hydrogen efficiency (over 15%) and suitable band edge positions for unassisted water splitting.

Ta_3N_5,[8c] $LaTiO_2N$,[8a] and $SrNbO_2N$[8b] photoelectrodes prepared by electrophoretic deposition (EPD) methods function as photoanodes for water oxidation. However, considerable water splitting photocurrents have only been achieved with Ta_3N_5 photoanodes, regardless of the fact that $LaTiO_2N$ and $SrNbO_2N$ materials can absorb comparable wavelengths of sunlight and possess similar band edge positions as Ta_3N_5. The easier reduction of Ti^{4+} and Nb^{5+} ions in comparison with Ta^{5+} during the high temperature ammonolysis process is considered to produce defects in the bulk and therefore result in less active $LaTiO_2N$ and $SrNbO_2N$ powders.[9] Optimizing the structure and crystallinity of $LaTiO_2N$ and $SrNbO_2N$ photoelectrodes may afford desirable improvements in PEC performance, considering that charge carrier transport among the film particles (or layers) depends largely on these parameters.[7c] Increasing photoelectrode crystallinity has been demonstrated to be effective in improving PEC performance by reducing the charge carrier recombination rate.[10] Efficient electron and hole transport rely on long-range film continuity and reduced hole transport distance, respectively, which require different film morphological characteristics.[11] It is desirable but always challenging to obtain highly crystalline interconnected particle film with small particle size.[3b]

Despite the above rules to follow and previous work on TaON and Ta_3N_5 photoanodes to refer to, obtaining highly photo-active $LaTiO_2N$ photoelectrodes (and more broadly, all the potentially available (oxy)nitride photoelectrodes) is still a great challenge, suggesting that charge transport limitations remain. The goal of this study is to define the limitations present in these (oxy) nitride photoelectrodes, using $LaTiO_2N$ as an example. Finally, we reveal that the poor electron transport associated with insufficient inter-particle connection contributes to the suppressed PEC activities of $LaTiO_2N$ photoanodes, which cannot be eliminated through necking treatment alone.[8c] Here, the

J. Y. Feng, W. J. Luo, T. Fang, H. Lv, Z. Q. Wang, J. Gao, W. M. Liu, Prof. T. Yu, Prof. Z. S. Li, Prof. Z. G. Zou
National Laboratory of Solid State Microstructures
College of Engineering and Applied Sciences
Ecomaterials and Renewable Energy Research Center
Nanjing University
22 Hankou Road, Nanjing 210093, China
E-mail: zsli@nju.edu.cn

DOI: 10.1002/adfm.201304046

PEC performances of $LaTiO_2N$ photoanodes are remarkably improved by constructing interconnected and single crystalline porous $LaTiO_2N$ particle film with greatly reduced amount of grain boundaries, thereby establishing an efficient charge carrier transport pathway among the film particles. The addition of hole scavengers allows us to assess the charge separation efficiencies of the $LaTiO_2N$ photoanodes and validates the advantages of the presently designed film characteristics. Upon surface modification by water oxidation catalysts (WOCs), the $LaTiO_2N$ photoanodes exhibit the highest solar photocurrents reported to date.

2. Results and Discussion

2.1. PEC Performance of Bare $LaTiO_2N$ Photoanodes

A polymerized complex (PC) method and solid-state reaction (SSR) were used to prepare the $La_2Ti_2O_7$ oxide. $LaTiO_2N$ particles were obtained upon nitridation of the oxide under an NH_3 flow and were deposited onto fluorine doped tin oxide (FTO) glass substrates using EPD.[8c] After post-necking treatment with $TiCl_4$ and heating under an NH_3 flow, the as-prepared $LaTiO_2N$ photoanodes were then evaluated for PEC water splitting. The as-obtained $LaTiO_2N$ samples are referred to as LTON SSR 1250 and LTON PC 1000, for example, based on their preparation conditions (LTON SSR 1250 means $LaTiO_2N$ is prepared from the solid-state reaction derived $La_2Ti_2O_7$ precursor, and the calcination temperature of the $La_2Ti_2O_7$ precursor is 1250 °C).

Figure 1 shows the photocurrent-potential curves of different $LaTiO_2N$ photoanodes measured in 0.1 M potassium phosphate (pH = 8, designated as KPi) electrolyte under visible-light irradiation ($\lambda \geq 420$ nm). The LTON PC 650 photoanode shows a negligible photocurrent of about 0.06 mA cm^{-2} at 1.8 V versus reversible hydrogen electrode (RHE), which is comparable

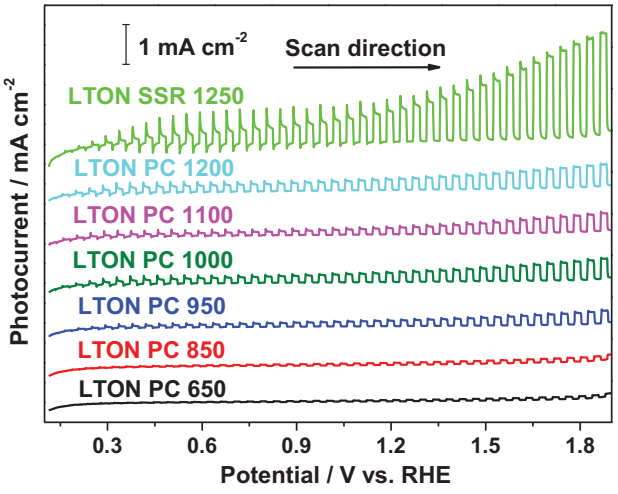

Figure 1. Photocurrents of different $LaTiO_2N$ photoanodes in 0.1 M KPi (pH = 8) electrolyte under visible-light irradiation ($\lambda \geq 420$ nm). The light source is a 500 W xenon lamp fitted with a cut-off filter (Hoya L-42); the scan rate is 30 mV s^{-1}.

with previous reports.[12] A slightly higher photocurrent of 0.1 mA cm^{-2} at 1.8 V_{RHE} is obtained for the LTON PC 850 photoanode. This enhancement of activity may be due to facilitated charge transport originating from increased crystallinity and/or better inter-particle connection of the $LaTiO_2N$ produced by calcination of the $La_2Ti_2O_7$ precursor at a higher temperature.[3b] This favorable enhancement proceeds with further increase in $La_2Ti_2O_7$ precursor calcination temperatures, affording photocurrents of 0.29 mA cm^{-2} for LTON PC 950 and 0.46 mA cm^{-2} for LTON PC 1000 at 1.8 V_{RHE}. Although further enhancement was expected, substantially larger photocurrents were not obtained for the LTON PC 1100 (0.4 mA cm^{-2}) and LTON PC 1200 (0.51 mA cm^{-2}) photoanodes at 1.8 V_{RHE}. These two samples were found to quickly settle out of suspension during the EPD process. As a result, the EPD biases were elevated to 20 V for LTON PC 1100 and 30 V for LTON PC 1200 samples, and the EPD time was reduced to 2 min (3 min showed no obvious difference). The resulting LTON PC 1100 and LTON PC 1200 photoanode films were thinner than the above films, and thus exhibited comparable photocurrents to that of the LTON PC 1000 photoanode.

2.2. Characterization of $LaTiO_2N$ Photoanodes and Particles

As expected, the X-ray diffraction (XRD) patterns of the $LaTiO_2N$ particles show more intense diffraction peaks at higher $La_2Ti_2O_7$ precursor calcination temperatures, indicating increasingly improved crystallinity (see Figure S1 in Supporting Information). Because crystal lattice defects usually act as recombination centers of photogenerated electrons and holes, increasing the crystallinity of the $LaTiO_2N$ photoelectrodes is expected to yield long-lived carriers. However, the increase in photocurrent is not proportional to the observed enhancement of crystallinity. The 4-fold performance improvement achieved for LTON SSR 1250 in comparison with that of LTON PC 1000 (2.34 mA cm^{-2} vs 0.46 mA cm^{-2} at 1.8 V_{RHE}) suggests the unambiguous contribution of the increased connection between film particles, alongside better crystallinity, to the facilitated electron transport. Therefore, poor electron transport may be the major charge transport limitation in $LaTiO_2N$ photoanodes prepared by the PC method. This is rational considering that calcination of the $La_2Ti_2O_7$ oxide precursor at high temperatures will promote sintering and necking of the oxide nanoparticles, leading to larger and better connected $LaTiO_2N$ particles.[3b]

The morphological characteristics of the $LaTiO_2N$ photoanodes were analyzed using field-emission scanning electron microscopy (FE-SEM). The inter-particle connection and the connection between the FTO substrate and the $LaTiO_2N$ particles are important for efficient charge carrier collection, these connections are ensured by the use of $TiCl_4$ necking agent. Because $TiCl_4$ treatment results in a partially covered film surface that hinders the clear observation of detailed structures (Figure S2, Supporting Information), the SEM images were recorded for the corresponding powders, except for the LTON SSR 1250 and LTON PC 1100 samples. **Figure 2**a shows that the average particle size of LTON PC 650 is about 50–80 nm, and that the particles are loosely aggregated to form large secondary particles (Figure S3a, Supporting Information). Slightly larger

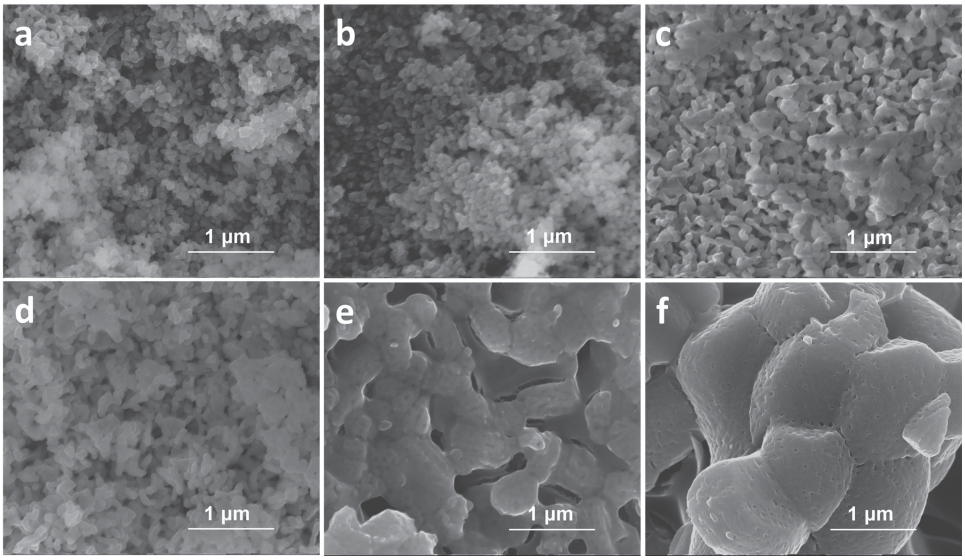

Figure 2. SEM images of a) LTON PC 650, b) LTON PC 850, c) LTON PC 950, d) LTON PC 1000, e) LTON PC 1100, and f) LTON SSR 1250 recorded from their corresponding photoanodes and powders. Except LTON PC 1100 and LTON SSR 1250 samples, the SEM images are recorded from their corresponding powders.

particles and correspondingly better adhesion among particles can be observed for the LTON PC 850 sample (Figure 2b). However, the relatively small voids among these nanoparticles prevented the sufficient penetration of $TiCl_4$ necking agent, resulting in poor electronic connection among the film particles and correspondingly poor photocurrents. At higher temperatures $La_2Ti_2O_7$ particle growth and coalescence occurred through inter-particle sintering and necking, which led to the formation of worm-like and rod-like particles for LTON PC 950 and LTON PC 1000 (Figure S2c,d, Supporting Information), and this favorable change for electron transport is immediately revealed by the increased photocurrents. The morphology further develops into macroporous aggregated particles with distinguishable small pores for LTON PC 1100 (Figure S2e, Supporting Information). These three-dimensionally interconnected porous particles are highly desirable for charge carrier transport and further increased performance was therefore expected. However, the enhancement of photocurrent was limited by the relatively reduced film thickness that resulted from the abrupt development of large particle sizes for LTON PC 1100 and LTON PC 1200 (Figure S3e–g, Supporting Information). The particles of LTON PC 1250 grew too large to fabricate its corresponding photoanode film by EPD. Accordingly, the above three samples failed to exhibit continuing improvement in PEC performance despite the better inter-particle connection and crystallinity.

For the preparation of complex (oxy)nitrides, PC is the optimal choice to fabricate oxide precursors because of the homogeneous distribution of constituent ions in the oxide precursor matrix. This, however, always produces loosely aggregated nanoparticles, making poor electron transport the major charge transport limitation present in the resulting (oxy)nitride photoanodes. Here we clearly point out the necessity of PC-prepared oxide precursors at high temperatures to form effective inter-particle connections among the final (oxy)nitride particles and thereby establish continuous electron transport pathways in the final (oxy)nitride photoelectrodes. The solid-state reaction always produces large particles with excellent crystallinity, which leads to good electron transport but poor hole transport because of the long hole migration distance. However, the macro- and mesopores concomitantly formed during the high temperature ammonolysis process endows SSR-derived $LaTiO_2N$ particles with three-dimensionally interconnected porous structures (shown in **Figure 3**). This largely decreases the hole migration distance while still maintaining outstanding electron transport. The formation of macro- and mesopores is induced by crystal shrinkage voids; three O^{2-} anions are replaced by two N^{3-} anions and the original particle size is maintained. The diverse crystal orientations observed in LTON PC 1100 indicate the presence of abundant grain boundaries, which may contribute to increased film resistance and electron-hole recombination. This hypothesis is supported by the slightly higher photocurrent observed for LTON PC 1200 compared with that for LTON PC 1100 despite the lower amount of particles of the former on the FTO substrate; a reduced number of grain boundaries is found in LTON PC 1200. In contrast, the large primary particles of LTON SSR 1250 are in single crystal form (shown in Figures 3b and Supporting Information, Figure S4), and aggregate tightly to form what are likely twin crystalline secondary particles with a sharply reduced number of grain boundaries. The formation of single crystalline porous $LaTiO_2N$ particles is based on topochemical conversion from the $La_2Ti_2O_7$ precursors.[13] The favorable characteristics of LTON SSR 1250, which include high crystallinity, a porous structure that allows sufficient contact area with the electrolyte while decreasing the hole transport distance, three-dimensionally interconnected single crystal particles, and a sharply reduced number of grain boundaries together contribute to its remarkably enhanced PEC performance by establishing an efficient charge carrier transport pathway among the film particles.[14]

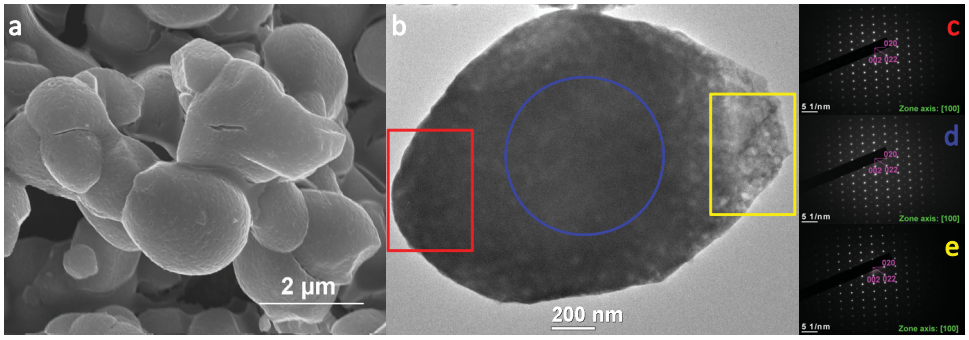

Figure 3. a) SEM image of LTON SSR 1250 showing the porous and tightly interconnected particle structure. b) Low-magnification transmission electron microscopy (TEM) image of a typical LTON SSR 1250 particle. The electron diffraction patterns taken from c) left, d) central, and e) right parts of the LTON SSR 1250 particle are almost identical, indicating that the whole particle is a porous single crystal.

2.3. Charge Transport Properties of $LaTiO_2N$ Photoanodes

Based on the SEM and TEM analysis, we show the effectiveness of establishing a charge carrier transport pathway among the film particles in sharply enhancing the photocurrents achieved by the $LaTiO_2N$ photoanodes. There is an urgent need to depict a more credible picture of the charge transport characteristics of $LaTiO_2N$ photoanodes in a quantitative way. The addition of an appropriate hole scavenger can completely suppress the surface recombination process to allow the quantitative assessment of the negative effects of surface and bulk recombination on PEC performance.[15] After testing various compounds (H_2O_2, $Fe(CN)_6^{4-}$, KI, Na_2SO_3), we have found Na_2SO_3 to be the optimal hole scavenger. As expected, LTON SSR 1250 exhibited a photocurrent about three times higher than that of the LTON PC 1000 photoanode in the presence of Na_2SO_3 within the potential range examined, and correspondingly about three times higher charge separation efficiency (shown in **Figure 4**). While the surface recombination process may not be completely suppressed when using Na_2SO_3 as a hole scavenger, the as-calculated charge separation efficiency can still give an assessment of the bulk charge transport loss. The greatly increased charge separation efficiency for the LTON SSR 1250 photoanode is in close agreement with our above hypothesis that highly photo-responsive $LaTiO_2N$ photoanodes can be achieved by establishing an efficient charge carrier transport pathway among the film particles. We also measured the photocurrents of the LTON SSR 1250 and LTON PC 1000 photoanodes with front-side and back-side illumination in the presence of Na_2SO_3. For the LTON PC 1000 photoanode, back-side illumination yielded a much higher photocurrent, suggesting that poor electron transport indeed limits its performance (Figure S5, Supporting Information). Comparatively, the LTON SSR 1250 photoanode exhibited comparable photocurrent densities for back-side and front-side illumination (Figure S6, Supporting Information), which is an indication that electron transport limitation has been largely ameliorated in the LTON SSR 1250 photoanode.[16,5b]

We conducted cross-sectional SEM analysis to further understand the charge transport processes occurring in the LTON SSR 1250 and LTON PC 1000 photoanodes. As shown in Figure 4c,d, both photoanode films have a similar thickness of about 2 μm, so the sharp difference in photocurrent between the LTON SSR 1250 and LTON PC 1000 photoanodes was not due to the amount of deposited $LaTiO_2N$ particles. The obvious difference between the two photoanodes is that the LTON SSR 1250 photoanode comprised tightly interconnected and porous single crystalline microparticles while the LTON PC 1000 photoanode was made up of loosely connected nanoparticles that suffered from insufficient penetration of $TiCl_4$ necking agent. The $TiCl_4$ necking agent was prevented from penetrating the voids among the LTON PC 1000 nanoparticles and instead formed a

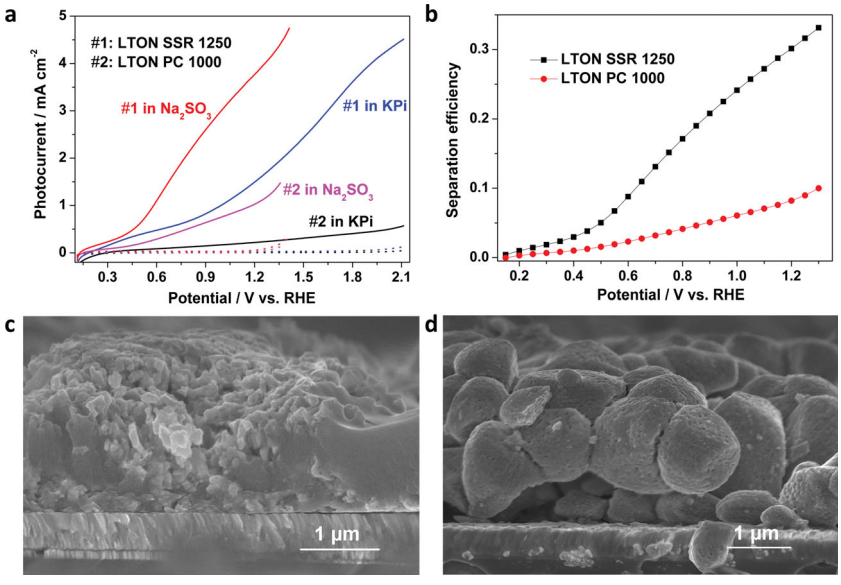

Figure 4. a) Photocurrents of the LTON SSR 1250 and LTON PC 1000 photoanodes in 0.1 M KPi (pH = 8) with and without 0.1 M Na_2SO_3. b) Charge separation efficiencies of the LTON SSR 1250 and LTON PC 1000 photoanodes at various applied voltages. The light source is AM 1.5 G simulated sunlight (100 mW cm^{-2}); the scan rate is 30 mV s^{-1}. c) Cross-sectional SEM image of the LTON PC 1000 photoanode. d) Cross-sectional SEM image of the LTON SSR 1250 photoanode.

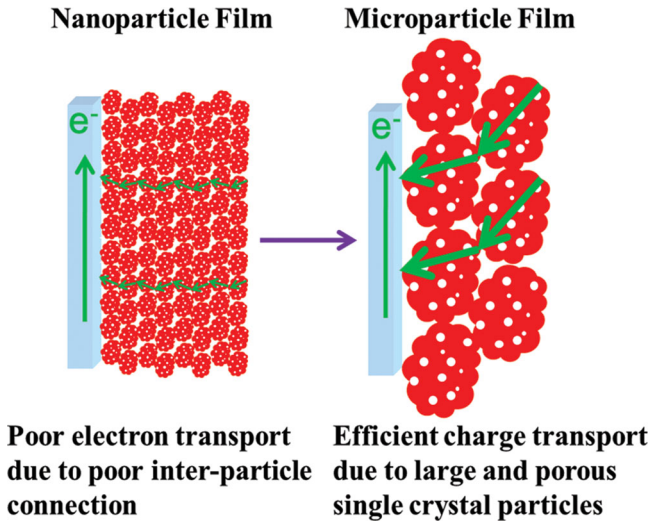

Figure 5. A proposed mechanism of facilitated charge transport in the LTON SSR 1250 photoanode.

liquid-like covering at the film edge. From Figure 4c, the presence of a large quantity of grain boundaries and poor interparticle connection contributed to the increased film resistance and electron-hole recombination. The use of three-dimensionally interconnected single crystalline and porous microparticles can greatly suppress these charge transport limitations. A proposed mechanism for this facilitated charge transport in the LTON SSR 1250 photoanode is shown in **Figure 5**.

Prior to this study, the intrinsic requirements for and significance of constituent (oxy)nitride particles for desirable PEC performances of (oxy)nitride photoelectrodes had not been noticed and investigated. Only TaON and Ta_3N_5 (prepared by the nitridation of commercial Ta_2O_5 of about 0.5–1 μm in particle size) were previously known to be available promising (oxy)nitride photoelectrode materials. However, it has not been clear why other suitable (oxy)nitrides (mostly prepared by the PC method because they usually consist of two or more metal ions) are inefficient because the previous work emphasizes the importance of necking treatment but not the particles themselves.[8c] In addition, the hole (the minority carrier) transport process is generally considered to be the major charge transport limitation in n-type semiconductors and has thus been carefully addressed by the use of well-crystalline and nanosized (oxy)nitride particles. It is now suggested that the performances of these suitable (oxy)nitride photoelectrodes are probably restricted by poor electron transport resulting from improper morphological characteristics of the corresponding films. Having obtained rules that permit efficient charge transport to follow, we are now encouraged to explore the substantial remaining (oxy)nitrides as potential photoelectrodes for solar energy conversion.

2.4. PEC Performance of Co_3O_4 Modified $LaTiO_2N$ Photoanodes

So far this work has provided a gradual increase of the plateau photocurrents of $LaTiO_2N$ photoanodes by addressing charge transport limitations. We now seek to improve the PEC performance of the present $LaTiO_2N$ photoanodes at lower bias through surface modification with Co_3O_4 WOC.[17] First, the effects of different electrolytes on the PEC performance of LTON SSR 1250 photoanode were investigated. Both KPi and NaOH electrolytes provide higher photocurrents than Na_2SO_4, with slightly greater enhancement observed for NaOH (Figure S7). Because the kinetic limitations to oxygen evolution originating from the low rate of proton removal in Na_2SO_4 are more pronounced after the surface deposition of WOC (Figure S8), we selected KPi and NaOH as the electrolytes. **Figure 6** represents the obtained photocurrent-voltage curves of the LTON SSR 1250 photoanodes with and without Co_3O_4 WOC under AM 1.5 G simulated sunlight (100 mW cm^{-2}). The LTON PC 1000 photoanode (shown for comparison) exhibits a photocurrent of about 0.5 mA cm^{-2} at 2 V_{RHE}, which is in accordance with a previous report.[8a] In sharp contrast, the LTON SSR 1250 photoanodes show substantially enhanced photocurrents, achieving 5.3 mA cm^{-2} in NaOH and 4.2 mA cm^{-2} in KPi at 2 V_{RHE}. The Mott-Schottky plots of the LTON SSR 1250 and LTON PC 1000 photoanodes show that they have a similar flat band potential (Figure S9, Supporting Information). As they exhibit a similar optical absorption edge, their band positions are also very similar (Figure S10, Supporting Information). This great advance in performance gives rise to the highest photocurrent ever reported for bare $LaTiO_2N$ photoanodes and makes $LaTiO_2N$ one of the most efficient photoanodes known. Unprecedented plateau photocurrents of about 6.5 mA cm^{-2} and over 4 mA cm^{-2} at 1.23 V_{RHE} have been obtained on the Co_3O_4/LTON SSR 1250 photoanodes, which is even larger than those reported for Co_3O_4/Ta_3N_5 photoanodes.[17] This result is readily reproducible on several repeat samples and about 7 mA cm^{-2} of plateau photocurrent can be achieved for the best samples. Our results therefore show not only a >2 mA cm^{-2} enhancement of plateau current compared with the best record obtained for well-optimized and precious IrO_2 modified $LaTiO_2N$ photoanodes prepared by a rather expensive and

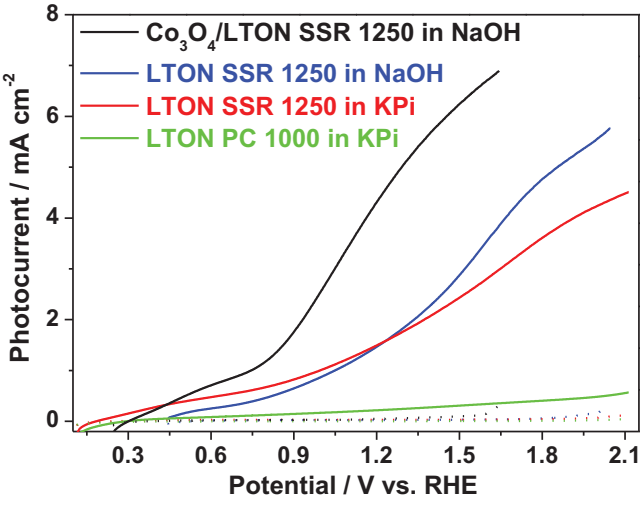

Figure 6. Photocurrents of LTON SSR 1250 photoanodes with and without surface modification by Co_3O_4 in 0.1 M KPi (pH = 8) and 1 M NaOH (pH = 13.6) electrolytes under AM 1.5 G 100 mW cm^{-2} simulated sunlight and scan rate of 30 mV s^{-1}. LTON PC 1000 without surface modification is also shown for comparison.

complex method, but also the important finding that poor electron transport is the performance-limiting process in $LaTiO_2N$.[18] In addition, although TiO_2 film was formed after the necking treatment as confirmed by XRD, it showed a negligible photocurrent under chopped simulated sunlight (Figures S11,S12, Supporting Information). Thus, the observed photocurrent was produced by water oxidation occurring mainly on the $LaTiO_2N$ particles.

We should point out that for a bare LTON SSR 1250 photoanode the plateau photocurrent is about 5.3 mA cm^{-2}, while for the Co_3O_4/LTON SSR 1250 photoanode the plateau photocurrent is about 6.5 mA cm^{-2}. About 45 s is needed to complete a linear sweep voltammetry with a scan rate of 30 mV s^{-1}, and we note that the photocurrents on a bare LTON SSR 1250 photoanode decrease substantially with successive scans (Figure S13, Supporting Information). So it is possible that Co_3O_4 modification partially inhibits the photodegradation of $LaTiO_2N$ during a linear sweep voltammetry, thus a slightly larger but photo-responsive current (not a capacitive current) is achieved. We have integrated the photocurrent density recorded during a linear sweep voltammetry with a scan rate of 30 mV s^{-1}. The charge passed through the outer circuit is about 129 mC cm^{-2}, which is at least 80 times higher than the amount of loaded Co (the amount of LTON SSR 1250 is about 1.5 μmol cm^{-2}, and the loaded Co is about 0.015 μmol cm^{-2} as estimated from the energy dispersive X-ray result, EDX). Therefore, the photocurrent after Co_3O_4 modification is mainly the oxidation of substrates by photogenerated holes but not solely the charging of Co_3O_4. The photocurrent-voltage curves of a Co_3O_4/LTON SSR 1250 photoanode with various scan rates are shown in Figure S14 (Supporting Information), which represent that the photocurrents on the Co_3O_4/LTON SSR 1250 photoanode do not change obviously with scan rates lower than 100 mV s^{-1}. At higher scan rates (200 mV s^{-1} and 500 mV s^{-1}), however, significantly increased photocurrents are observed, which are probably related with the capacitive charging of both LTON SSR 1250 and Co_3O_4 at the solid-liquid interface (Figures S15,S16, Supporting Information). With a scan rate of 10 mV s^{-1} a slightly lower photocurrent on the Co_3O_4/LTON SSR 1250 photoanode is obtained, which is demonstrated to be due to the photodegradation of $LaTiO_2N$ by sweeping the Co_3O_4/LTON SSR 1250 photoanode with a scan speed of 30 mV s^{-1} again and reproducing the photocurrent-voltage curve as that of 10 mV s^{-1}. Sustained scans of the Co_3O_4/LTON SSR 1250 photoanode with a rate of 30 mV s^{-1} reveal that there is detectable photocurrent decay on the LTON SSR 1250 photoanode, even with the Co_3O_4 WOC modification.

2.5. Photocurrent Action Spectra and Photostability of a Co_3O_4 Modified $LaTiO_2N$ Photoanode

To verify the above photocurrents under AM 1.5 G simulated sunlight condition (100 mW cm^{-2}), the incident photon to current efficiency (IPCE) has been measured under monochromatic light irradiation and plotted as a function of wavelength at various voltages (**Figure 7**). For the bare LTON SSR 1250 photoanode, obsessed by the problem of photoinstability its IPCE measurement is omitted. During the IPCE measurement the light intensity is about 1–2 mW cm^{-2}, under this condition the

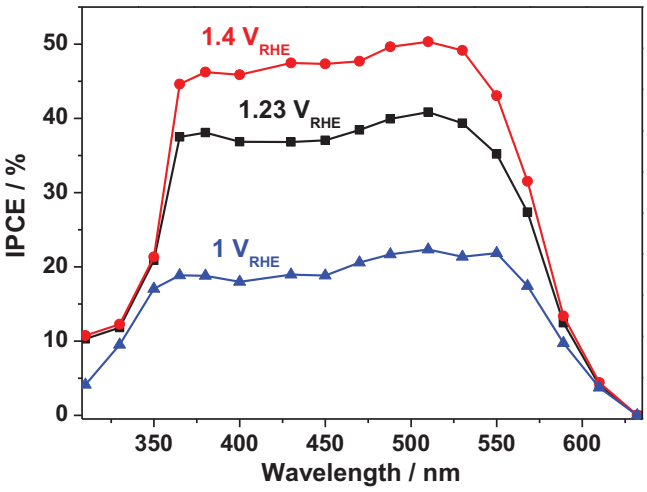

Figure 7. Incident photon to current efficiency (IPCE) spectra of the same Co_3O_4/LTON SSR 1250 electrode at 1.4 V_{RHE}, 1.23 V_{RHE}, 1 V_{RHE} as a function of wavelength. All the data are collected in 1 M NaOH solution (pH = 13.6).

photodegradation of the Co_3O_4/LTON SSR 1250 photoanode is negligible and the photocurrents are fully reproducible, thus allowing relatively accurate assessment of PEC performance of the Co_3O_4/LTON SSR 1250 photoanode. The IPCE values on the Co_3O_4/LTON SSR 1250 photoanode at 1.23 V_{RHE} are about 36% in the wavelength range from 365 to 550 nm, which are larger than that of the Co_3O_4/Ta_3N_5 photoanodes[17] and have fairly exceeded the previous report on the bare $LaTiO_2N$ photoanode.[8a] Multiplication of the obtained IPCE spectrums with standard solar spectral distribution yields the solar photocurrent spectrums at different biases, which are integrated with respect to the wavelength to give the predicted photocurrents of 5.4 mA cm^{-2} at 1.4 V_{RHE}, 4.4 mA cm^{-2} at 1.23 V_{RHE} and 2.5 mA cm^{-2} at 1 V_{RHE}, respectively (Figure S17, Supporting Information). The small differences between the calculated and tested photocurrents indicate the IPCE values and photocurrents under AM 1.5 G sunlight are credible.

Finally, the photostability of a Co_3O_4/LTON SSR 1250 photoanode (active area is about 0.8 cm^2) is tested under AM 1.5 G simulated sunlight condition (100 mW cm^{-2}) at 1.23 V_{RHE}. After 2.5 h irradiation the photocurrent on the Co_3O_4/LTON SSR 1250 photoanode decreases to be about 0.5 mA, with a sharp decrease in the initial period followed by a gradual decay (**Figure 8**a). Dark for a time interval of several seconds and illuminating the photoanode again cannot fully recover the photocurrent, indicating the irreversible self-oxidative decomposition of $LaTiO_2N$ has occurred. The element mapping of cobalt on the large scales of the Co_3O_4/LTON SSR 1250 electrode and SEM analysis reveal uniform distribution of Co_3O_4 nanoparticles on the surface of LTON SSR 1250 particles (Figure S18, Supporting Information). Although with this favorable distribution of Co_3O_4 WOC on the outer surface of LTON SSR 1250 particles, the inner pores of LTON SSR 1250 particles are exposed to electrolyte thus suffer from photodegradation, as the present loading method of Co_3O_4 WOC cannot afford the deposition of Co_3O_4 WOC on the inner surface of LTON SSR 1250 particles. Further improvement of photostability will resort to

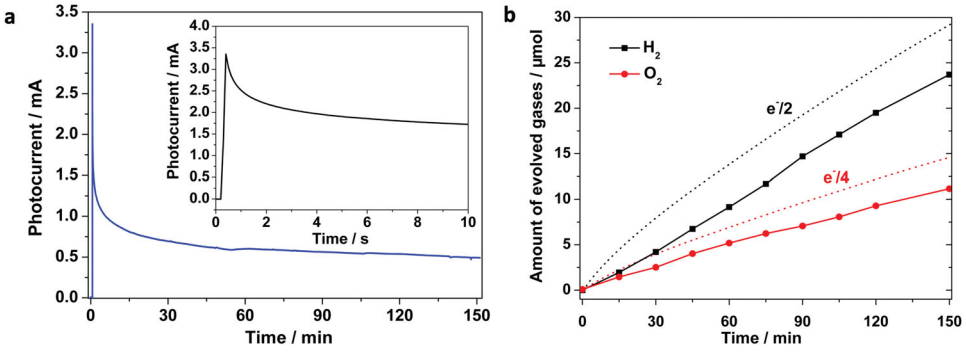

Figure 8. a) Photocurrent decay curve measured at 1.23 V_{RHE} under AM 1.5 G 100 mW cm^{-2} simulated sunlight for a Co_3O_4/LTON SSR 1250 photoelectrode (0.8 cm^2) in 1 M NaOH (pH = 13.6) solution. Inset: Photocurrent decay curve at the initial period of 10 s. b) Time course of gas evolution under the condition corresponding to (a). Dashed lines correspond to faradaic efficiency of 100%.

optimization of WOCs loaded on the $LaTiO_2N$ photoanodes or proper surface protection layer.[19] The integration of photocurrent decay curve of the Co_3O_4/LTON SSR 1250 photoanode shows that 5.66 C of electrons has passed through the circuit during 2.5 h measurement, corresponding to 58.6 µmol of electrons. The amount of LTON SSR 1250 is about 1.2 µmol, so the majority of photocurrent on the Co_3O_4/LTON SSR 1250 photoanode is associated with water oxidation, not merely caused by the self-oxidative decomposition of the $LaTiO_2N$ itself. We have also monitored the amount of evolved gases during the photocurrent-time measurement on the Co_3O_4/LTON SSR 1250 photoanode (Figure 8b). The faradaic efficiencies for O_2 and H_2 production are 76% and 80%, respectively, indicating the possible contribution of water formation from produced H_2 and O_2 on the Pt foil in the present single-compartment cell.

Comparing with the previous reports,[8a,18] our Co_3O_4/LTON SSR 1250 photoanode is demonstrated to be the most stable $LaTiO_2N$ photoanode, with a reliable faradaic efficiency of water decomposition. As we presently cannot obtain stable photocurrents on the Co_3O_4/LTON SSR 1250 photoelectrodes, the calculation of applied bias photon-to-current efficiencies is omitted. Unlike stable metal oxide photoanodes, the biggest obstacle for the practical utilization faced by (oxy)nitride photoelectrodes (after our present efforts) is their photochemical stabilities, which, however, needs extensive and sufficient investigations of the loading strategies and types of WOCs. Only when the kinetics of water oxidation is properly accelerated, the harmful competing reaction of N anions oxidation in lattice by photogenerated holes will be fully excluded, achieving efficient and stable PEC water splitting on the (oxy)nitride photoelectrodes, which is a longstanding and arduous task in the future.

3. Conclusions

For the first time, we show the particular requirements for efficient charge transport among (oxy)nitride particles in the resulting film, and report the correspondingly improved PEC performances of $LaTiO_2N$ photoanodes. By establishing highly crystalline porous $LaTiO_2N$ particles and superior inter-particle connectivity with reduced density of grain boundaries among the film particles, a plateau photocurrent of about 6.5 mA cm^{-2} on Co_3O_4/$LaTiO_2N$ photoanodes has been demonstrated under simulated sunlight. This photocurrent value is the highest reported for $LaTiO_2N$ photoanodes and is comparable with that of Co_3O_4/Ta_3N_5 photoanodes. Given the generality of our strategy, this study also shows promising potential for the tremendous numbers of unexplored (oxy)nitrides photoelectrodes for future solar energy conversion.

4. Experimental Section

Preparation of $LaTiO_2N$ Particles: $La_2Ti_2O_7$ precursors were prepared by the polymerized complex (PC) method and the solid state reaction (SSR). For the PC method, stoichiometric amount of $Ti[OCH(CH_3)_2]_4$ (titanium tetraisopropoxide) and $La(NO_3)_3{\cdot}6H_2O$ were dissolved in ethylene glycol, after which citric acid and methanol were added into the above solution under stirring. The mixture was kept at 150 °C to promote polymerization. After becoming a transparent resin, the mixture was pyrolyzed at 350 °C for 1 h, followed by calcination in air at 650 °C for 2 h to remove the carbon. The white powders were then calcined at different temperatures (850 °C, 950 °C, 1000 °C, 1100 °C, 1200 °C, and 1250 °C) for 10 h to promote the sintering and necking of the oxide nanoparticles. For the SSR method, stoichiometric amount of TiO_2 and La_2O_3 were mixed with appropriate amount of ethanol, after which the mixture was heated at 800 °C for 2 h and 1250 °C for 10 h, respectively, with intermediate grinding. $LaTiO_2N$ particles were obtained by heating corresponding $La_2Ti_2O_7$ powders (0.5 g) at 950 °C for 15 h under a flow of ammonia gas (flow rate: 200 mL min^{-1}). The as-obtained $LaTiO_2N$ powders are referred to LTON SSR 1250 and LTON PC 1000 for example, respectively, based on the preparation conditions.

Fabrication of $LaTiO_2N$ Photoanodes: $LaTiO_2N$ photoanodes were fabricated using electrophoretic deposition (EPD) method followed by necking treatment. Typically, iodine (5 mg) and $LaTiO_2N$ (20 mg) powder were dispersed in acetone (25 mL) with the assistance of sonication to obtain the $LaTiO_2N$ powder suspension for EPD.[8] The EPD process was conducted between two parallel FTO electrodes with the distance of 1 cm under 10 V of bias for 3 min. As the $LaTiO_2N$ powders exhibit different sizes, the EPD bias for LTON PC 1100 was 20 V, for LTON PC 1200 and LTON SSR 1250 was 30 V, and the EPD time was 2 minutes. The coated area of the $LaTiO_2N$ film was ca. 1 cm × 1 cm. The electrodes were dried in air, and then dropped with $TiCl_4$ methanol solution (50 mM, 30 µL). Finally, the dropped electrodes were heated at 500 °C for 30 min (NH_3 flow rate: 500 mL min^{-1}).

Deposition of Co_3O_4 Water Oxidation Catalyst (WOC) on $LaTiO_2N$ Photoanodes: The deposition of Co_3O_4 WOC onto the $LaTiO_2N$ photoanodes was carried out by an impregnation method as the previous procedures.[17] The colloidal $Co(OH)_x$ solution was firstly prepared by the addition of NaOH into an aqueous solution containing Co^{2+} ions. The $LaTiO_2N$ electrodes were then immersed into the as

prepared $Co(OH)_x$ colloidal solution for 1 h, washed with distilled water and then dried in air. Finally, $Co(OH)_x$ on the $LaTiO_2N$ electrodes were calcined at 300 °C for 10 min in air to form Co_3O_4 WOC.

Photoelectrochemical Characterization: Photoelectrochemical measurements were carried out in a three-electrode configuration cell using an aqueous hydroxide electrolyte (1 M NaOH, pH = 13.6), with $LaTiO_2N$ film as the working electrode, Hg/Hg_2Cl_2 in saturated KCl as the reference electrode, and Pt foil as the counter electrode. Potentials are reported vs. reversible hydrogen electrode (RHE). In this experiment, 0.1 M potassium phosphate (pH = 8, designated as KPi) and 0.5 M Na_2SO_4 (pH = 8) were also used as electrolytes. Photocurrent densities under visible-light irradiation were obtained by using a 500 W xenon lamp fitted with a cut-off filter (Hoya L-42). AM 1.5 G simulated sunlight (100 mW cm^{-2}) was obtained from a Newport Sol3A Class AAA simulator. The light intensity of the sunlight simulator was calibrated at 100 mW cm^{-2} by the standard reference of a Newport 91150 silicon cell before each use. The irradiated area was circular with a diameter of ≈6 mm and photocurrent densities were normalized to 1 cm^2. The incident photon to current efficiency (IPCE) was measured under monochromatic light irradiation, provided by the xenon lamp equipped with band pass filters. The light intensity was obtained with a photometer (Newport, 840-C), being 1–2 mW cm^{-2}. The charge separation efficiency is obtained by dividing J_{abs} (photocurrent density assuming 100% conversion efficiency of absorbed photons, and about 12.5 mA cm^{-2} is estimated for $LaTiO_2N$) by J_{sep} (photocurrent density assuming 100% conversion efficiency of holes reaching the electrode/electrolyte interface, and in the present case the photocurrent density in the presence of Na_2SO_3).

Sample Characterization: The crystal structures of all the samples were measured by powder X-ray diffraction (XRD, Rigaku Ultima III) with Cu Kα radiation (λ = 1.54056 Å). The optical absorption spectra of the $LaTiO_2N$ samples were performed on an UV-visible (UV-VIS) spectrophotometer (Shimadzu, UV-Vis 2550). The morphology of the $LaTiO_2N$ photoanodes and powders was observed by field-emission scanning electron microscopy (FE-SEM; Nova NanoSEM 230, FEI), and no conductive coating was deposited onto samples for these SEM measurements. TEM analysis was performed on a high-resolution transmission electron microscope (JEM-2100).

Product Analysis: The evolved gases were detected using a gas chromatograph (Agilent 490 Micro GC). High-purity Ar was purged into a closed single-compartment PEC cell for about 30 min to remove O_2 before the illumination. The three-electrode configuration was used and the area of the Co_3O_4/LTON SSR 1250 photoelectrode was about 0.8 cm^2. The electrolyte was 1 M NaOH and the light was AM 1.5 G simulated sunlight (100 mW cm^{-2}).

Supporting Information

Supporting Information is available from the Wiley Online Library or from the author.

Acknowledgements

This work was financially supported by 973 Program (No. 2013CB632404), a Project Funded by the Priority Academic Program Development of Jiangsu Higher Education Institutions, NCET-12–0268, and NSFC (nos. 51272102, 21073090, and 51272101).

Received: December 2, 2013
Revised: January 20, 2014
Published online: February 28, 2014

[1] a) M. Grätzel, *Nature* **2001**, *414*, 338; b) N. S. Lewis, D. G. Nocera, *Proc. Natl. Acad. Sci. U.S.A.* **2006**, *103*, 15729; c) O. Khaselev, J. A. Turner, *Science* **1998**, *280*, 425; d) Z. Li, W. Luo, M. Zhang, J. Feng, Z. Zou, *Energy Environ. Sci.* **2013**, *6*, 347.
[2] A. Fujishima, K. Honda, *Nature* **1972**, *238*, 37.
[3] a) S. D. Tilley, M. Cornuz, K. Sivula, M. Grätzel, *Angew. Chem. Int. Ed.* **2010**, *49*, 64058; b) J. Brillet, M. Grätzel, K. Sivula, *Nano Lett.* **2010**, *10*, 4155; c) M. Zhang, W. Luo, Z. Li, T. Yu, Z. Zou, *Appl. Phys. Lett.* **2010**, *97*, 042105; d) K. Sivula, F. Le Formal, M. Grätzel, *ChemSusChem* **2011**, *4*, 432; e) Y. Lin, G. Yuan, S. Sheehan, S. Zhou, D. Wang, *Energy Environ. Sci.* **2011**, *4*, 4862; f) S. C. Warren, K. Voïtchovsky, H. Dotan, C. M. Leroy, M. Cornuz, F. Stellacci, C. Hébert, A. Rothschild, M. Grätzel, *Nat. Mater.* **2013**, *12*, 842; g) J. Sun, D. K. Zhong, D. R. Gamelin, *Energy Environ. Sci.* **2010**, *3*, 1252; h) Y. Ling, G. Wang, J. Reddy, C. Wang, J. Z. Zhang, Y. Li, *Angew. Chem. Int. Ed.* **2012**, *51*, 4074.
[4] B. D. Alexander, P. J. Kulesza, L. Rutkowska, R. Solarska, J. Augustynski, *J. Mater. Chem.* **2008**, *18*, 2298.
[5] a) F. F. Abdi, R. van de Krol, *J. Phys. Chem. C* **2012**, *116*, 9398; b) W. Luo, Z. Yang, Z. Li, J. Zhang, J. Liu, Z. Zhao, Z. Wang, S. Yan, T. Yu, Z. Zou, *Energy Environ. Sci.* **2011**, *4*, 4046.
[6] a) M. Hara, G. Hitoki, T. Takata, J. N. Kondo, H. Kobayashi, K. Domen, *Catal. Today* **2003**, *78*, 555; b) M. Y. Liu, W. S. You, Z. B. Lei, G. H. Zhou, J. J. Yang, G. P. Wu, G. J. Ma, G. Y. Luan, T. Takata, M. Hara, K. Domen, C. Li, *Chem. Commun.* **2004**, 2192; c) Z. Wang, J. Hou, S. Jiao, K. Huang, H. Zhu, *J. Mater. Chem.* **2012**, *22*, 21972.
[7] a) H. X. Dang, N. T. Hahn, H. S. Park, A. J. Bard, C. B. Mullins, *J. Phys. Chem. C* **2012**, *116*, 19225; b) Y. Cong, H. S. Park, S. Wang, H. X. Dang, F. F. Fan, C. B. Mullins, A. J. Bard, *J. Phys. Chem. C* **2012**, *116*, 14541; c) B. A. Pinaud, P. C. K. Vesborg, T. F. Jaramillo, *J. Phys. Chem. C* **2012**, *116*, 15918; d) Y. Kado, C. Lee, K. Lee, J. Mueller, M. Moll, E. Spiecker, P. Schmuki, *Chem. Commun.* **2012**, *48*, 8685; e) Y. Kado, R. Hahn, C. Lee, P. Schmuki, *Electrochem. Commun.* **2012**, *17*, 67.
[8] a) C. M. Leroy, A. E. Maegli, K. Sivula, T. Hisatomi, N. Xanthopoulos, E. H. Otal, S. Yoon, A. Weidenkaff, R. Sanjines, M. Grätzel, *Chem. Commun.* **2012**, *48*, 820; b) K. Maeda, M. Higashi, B. Siritanaratkul, R. Abe, K. Domen, *J. Am. Chem. Soc.* **2011**, *133*, 12334; c) M. Higashi, K. Domen, R. Abe, *Energy Environ. Sci.* **2011**, *4*, 4138.
[9] D. Logvinovich, A. Börger, M. Döbeli, S. G. Ebbinghaus, A. Reller, A. Weidenkaff, *Prog. Solid State Chem.* **2007**, *35*, 281.
[10] J. Cao, T. Kako, P. Li, S. Ouyang, J. Ye, *Electrochem. Commun.* **2011**, *13*, 275.
[11] a) X. J. Feng, T. J. LaTempa, J. I. Basham, G. K. Mor, O. K. Varghese, C. A. Grimes, *Nano Lett.* **2010**, *10*, 948; b) Y. Sun, H. Cheng, S. Gao, Z. Sun, Q. Liu, Q. Liu, F. Lei, T. Yao, J. He, S. Wei, Y. Xie, *Angew. Chem. Int. Ed.* **2012**, *51*, 8727.
[12] a) N. Nishimura, B. Raphael, K. Maeda, L. Le Gendre, R. Abe, J. Kubota, K. Domen, *Thin Solid Films* **2010**, *518*, 5855; b) C. Le Paven-Thivet, A. Ishikawa, A. Ziani, L. Le Gendre, M. Yoshida, J. Kubota, F. Tessier, K. Doment, *J. Phys. Chem. C* **2009**, *113*, 6156.
[13] a) S. G. Ebbinghaus, R. Aguiar, A. Weidenkaff, S. Gsell, A. Reller, *Solid State Sci.* **2008**, *10*, 709; b) F. Zhang, A. Yamakata, K. Maeda, Y. Moriya, T. Takata, J. Kubota, K. Teshima, S. Oishi, K. Domen, *J. Am. Chem. Soc.* **2012**, *134*, 8348.
[14] E. J. W. Crossland, N. Noel, V. Sivaram, T. Leijtens, J. A. Alexander-Webber, H. J. Snaith, *Nature* **2013**, *495*, 215.
[15] H. Dotan, K. Sivula, M. Grätzel, A. Rothschild, S. C. Warren, *Energy Environ. Sci.* **2011**, *4*, 958.
[16] a) D. K. Zhong, S. Choi, D. R. Gamelin, *J. Am. Chem. Soc.* **2011**, *133*, 18370; b) J. A. Seabold, K. Choi, *J. Am. Chem. Soc.* **2012**, *134*, 2186.
[17] M. Liao, J. Feng, W. Luo, Z. Wang, J. Zhang, Z. Li, T. Yu, Z. Zou, *Adv. Funct. Mater.* **2012**, *22*, 3066.
[18] T. Minegishi, N. Nishimura, J. Kubota, K. Domen, *Chem. Sci.* **2013**, *4*, 1120.
[19] a) A. Paracchino, V. Laporte, K. Sivula, M. Grätzel, E. Thimsen, *Nat. Mater.* **2011**, *10*, 456; b) Y. W. Chen, J. D. Prange, S. Dühnen, Y. Park, M. Gunji, C. E. D. Chidsey, P. C. McIntyre, *Nat. Mater.* **2011**, *10*, 539.